# Dielectric and Sorption Responses of Hydrogen-Bonding Network of Amorphous $C_{60}(OH)_{12}$ and $C_{60}(OH)_{36}$

*Shota Uchikawa,[†] Ayumi Kawasaki,[†] Norihisa Hoshino,[†,‡] Takashi Takeda,[†,‡] Shin-ichiro Noro,*[#] Kiyonori Takahashi,[¶] Takayoshi Nakamura,[¶] Nozomi Sato,[±] Ken Kokubo,[±] Hidehiro Sakurai,[±] Tomoyuki Akutagawa*[†,‡]*

[†] Graduate School of Engineering, Tohoku University, Sendai 980-8579, Japan. [‡] Institute of Multidisciplinary Research for Advanced Materials (IMRAM), Tohoku University, 2-1-1 Katahira, Aoba-ku, Sendai 980-8577, Japan. [#] Faculty of Environmental Earth Science, Hokkaido University, Sapporo 060-0810, Japan. [¶] Research Institute for Electronic Science, Hokkaido University, Sapporo 001-0020, Japan. [±] Graduate School of Engineering, Osaka University, Suita, Osaka 565-0871, Japan.

**RECEIVED DATE (to be automatically inserted after your manuscript is accepted if required according to the journal that you are submitting your paper to)**

Institute of Multidisciplinary Research for Advanced Materials (IMRAM), Tohoku University, 2-1-1 Katahira, Aoba-ku, Sendai 980-8577, Japan

Phone: +81-22-217-5653

Fax: +81-22-217-5655

E-mail akutagawa@tohoku.ac.jp

**Abstract**: Hydrophilic fullerene derivatives of $C_{60}(OH)_{12}$ (**1**) and $C_{60}(OH)_{36}$ (**2**) bearing different numbers of –OH groups formed amorphous solids of **1**•x($H_2O$) (x = 5–10) and **2**•x($H_2O$) (x = 15–22), respectively, according to the humidity. The thermally activated dynamic molecular motion of polar $H_2O$ was confirmed in the DSC and dielectric spectra. Three-dimensional O-H•••O hydrogen-bonding networks in amorphous **1** and **2** produced extrinsic adsorption-desorption pores with a hydrophilic environment posed by -OH groups, where $N_2$, $CO_2$, $H_2$, and $CH_4$ gases vapors and polar $H_2O$, MeOH, and EtOH molecules reversibly adsorbed into the networks. Molecular motion of polar $H_2O$ was directly observed in dielectric enhancement and protonic conductivity in three-dimensional O-H•••O hydrogen-bonding networks. The Brunauer-Emmett-Teller (BET) specific surface areas of amorphous **1** and **2** were 315 and 351 $m^2\ g^{-1}$, respectively, from the $CO_2$ sorption isotherms. Reversible vapor sorption behaviors with structural changes of amorphous **1** and **2** were also confirmed for the polar $H_2O$, MeOH, and EtOH.

## 1. Introduction

Porous materials, such as zeolites and carbons, have attracted much attention toward utilizing their high performance and selective storage, separation, and purification for global warming gases, clean energy, high energy, etc.[1-4] Inorganic porous materials have uniform intrinsic nanopores and/or mesopores to selectively capture the target gases. Recently, chemically designable and structurally diverse metal-organic frameworks (MOFs), porous coordination polymers, and covalent organic frameworks (COFs) have been applied to design pores and provide additional functionalities.[5-9] Although the structural diversity of organic ligands and monomer molecules drastically enhanced the number of such porous materials, one of the disadvantages of these materials is their low solubility in common organic solvents and low processability to fabricate thin films. To solve this, a new fabrication technique for MOF/COF thin films has been developed using the layer-by-layer technique.[10-14] In contrast, much attention has focused toward low-molecular-weight (LMW) organic sorption materials because of their high processability for thin-film devices using wet-fabrication techniques, such as drop-casting and spin-coating methods, because LMW organic compounds have a high solubility in common organic solvents.[15-17] Recently, the liquid-liquid interface has been utilized for thin film fabrication, resulting in gas-transport free-standing thin films composed of a supramolecular organic framework (SOF) using the porous organic cage molecule on the porous alumina substrate.[18-23] The molecular assembly structures of SOF were constructed based on weak intermolecular hydrogen-bonding and van der Waals interactions.

Although LMW organic compounds usually form the closest packing structures in solids with the absence of pores, two kinds of approaches to obtain the intrinsic and extrinsic pores within the crystalline materials have been used to design a reversible adsorption-desorption crystalline environment.[15-17] The former intrinsic pores of LMW organic compounds have been reported in calix[4]arene,[18-23] [4+6]cycloimine cages,[24-29] cucurbit[6]uril,[30-31] etc.,[32-39] whose intrinsic nanopores can be utilized as adsorption-desorption environments for gaseous $CO_2$, $N_2$, $H_2$, and $CH_4$. In contrast, the extrinsic pores of LMW organic compounds of tris(*o*-phenylenedioxy)cyclotriphosphazene,[40-41] 3,3',4,4'-

tetra(trimethylsilylethynyl)biphenyl,[42] triptycenetrisbenzimidazolone,[43] and others,[44-51] can be reversibly formed by removing the crystallization solvents. Recent Brunauer-Emmett-Teller (BET) specific surface areas of LMW organic compounds exceeded 3000 $m^2 g^{-1}$ for a triptycenetrisbenzimidazolone derivative,[43] where the chemical designs of weak intermolecular hydrogen-bonding and van der Waals interactions play essential roles in achieving structurally flexible packing structures. Structural reconstruction of the molecular arrangements of LMW organic compounds can form reversible molecular and gas sorption environments within the crystals.

Single crystalline LMW organic compounds, including crystallization solvents, are candidates to form extrinsic molecular and gas sorption pores within the crystals. In the crystalline porous materials, the long-range periodicity of the crystal lattice should be maintained after the removal of solvent molecules, where the molecules and gases can diffuse into the pores of the crystal lattice. The softness and robustness of the crystal lattice are important considerations to obtain LMW organic sorption materials. Recent examinations of intrinsic-cage-type molecules have focused on compounds with large BET specific surface areas, specific chiral recognition pores,[52] and possible thin film fabrication.[53] Development of new types of materials should be considered to expand the variation of LMW organic sorption materials because the molecular design strategy for LMW organic sorption materials is not sufficiently established.

The molecular assembly states of LMW organic sorption materials are another important consideration that affects the deterioration properties of vapor and gas-phase adsorption-desorption cycles. The sorption cycle of amorphous organic materials is much robust than those of single crystalline ones. Such amorphous materials have been widely applied in the fields of device fabrication, e.g., for ferroelectric relaxers,[54] organic transitions,[55] and organic electro luminescence.[56-57] In the field of LMW organic sorption materials, the $CO_2$ adsorption property has been reported for the intrinsic pores of amorphous cucurbit[7]uril derivatives and noria.[58-59] The formation of extrinsic pores has not been reported for amorphous LMW organic sorption materials.

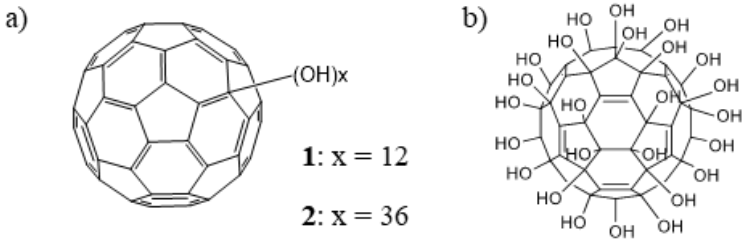


**Scheme 1.** Molecular structures of a) $C_{60}(OH)_x$ (**1**: x = 12 and **2**: x = 36) and b) a possible isomer of $C_{60}(OH)_{36}$.

Polyhydroxylated hydrophilic fullerene derivatives of $C_{60}(OH)_x$ (x = 12–44) are easily soluble in water, depending on the average number of hydroxyl groups as a mixture of many isomers, whereby the number of –OH groups (x) on the $C_{60}$ surface modify the hydrophilicity and the magnitude of the intermolecular O-H•••O hydrogen-bonding interactions.[60-63] Although the water soluble uniform nanosphere with an average diameter of approximately 1 nm has been utilized for chemical mechanical polishing of slurries[62-63] and antioxidants because of the free radical scavenging activity,[64-68] molecular assembly structures and physical properties of solid state $C_{60}(OH)_x$ have not been sufficiently examined. The high affinity for the water and hydrogen-bonding interactions of $C_{60}(OH)_x$ have the potential to show interesting physical responses coupled with hydrogen-bonding interactions. Herein, two kinds of $C_{60}(OH)_x$ derivatives, i.e., $C_{60}(OH)_{12}$ (**1**) and $C_{60}(OH)_{36}$ (**2**), with different hydrophilicities and hydrogen-bonding abilities were examined in terms of molecular assemblies, proton dynamics, dielectric responses, vapor and gas adsorption-desorption behaviors for $H_2O$, MeOH, EtOH, $N_2$, $CO_2$, $H_2$, and $CH_4$ as a new candidate for LMW organic sorption materials with extrinsic hydrogen-bonding network pores (Scheme 1). Although small molecules, such as $H_2$, $N_2$, and $H_2O$, can be captured in the internal space of the spherical $C_{60}$ π-plane, these molecules cannot pass through the outside π-plane of $C_{60}$ under ambient conditions.[69-71] In contrast, the superconducting transition temperature of 33 K has been reported for a 3:1 salt of $Cs^+$:$C_{60}$,

whose crystal structure is that of the closest-packing structure, i.e., the face-centered cubic lattice.[72-73] The occupation volumes of three molar $Cs^+$ ions and $C_{60}$ are approximately 59 and 540 $Å^3$, respectively, because the ionic and van der Waals radii of $Cs^+$ and $C_{60}$ are 1.67 and 5.05 Å, respectively. Therefore, the closest-packing structure of $C_{60}$ has a relatively large external pore size (>10% of the volume of $C_{60}$), which can be utilized for the molecular adsorption-desorption environment.

## 2. Experimental Section

**2.1. Physical measurements.** Infrared (IR, 400–4000 $cm^{-1}$) spectra were measured on a KBr pellet using a Thermo Fisher Scientific Nicolet 6700 spectrophotometer with a resolution of 4 $cm^{-1}$. The in situ IR measurements under $CO_2$ were performed using an Oxford cryostat MicrostatN with a neat sample under the control of $CO_2$ pressure at 195 K. Thermogravimetric (TG) differential thermal analysis and differential scanning calorimetry (DSC) were conducted using a Rigaku Thermo plus TG8120 thermal analysis station and Mettler DSC1-T with an $Al_2O_3$ reference and a heating and cooling rate of 5 K $min^{-1}$ under nitrogen. The temperature-dependent dielectric constants were measured using the two-probe AC impedance method from 1 kHz to 1 MHz (Hewlett-Packard, HP4194A) and the temperature controller of a Linkam LTS-E350 system. The electrical contacts were prepared using gold paste (Tokuriki 8560) to attach the 25-μm ϕ gold wires to the 3-mm ϕ compressed pellet. Temperature-dependent powder X-ray diffraction (PXRD) was performed using a Rigaku SmartLab diffractometer with Cu K$\alpha$ ($\lambda$ = 1.54187 Å) radiation.

**2.2. Preparation of 1 and 2.** Polyhydroxylated fullerene $C_{60}(OH)_{12}$ (**1**) was used as purchased from Frontier Carbon Corporation as nanom spectra D100. The supplier claims an average number of hydroxyl of ~10 by preparation with a modified synthetic method to give $C_{60}(OH)_{12}$.[62-63] Polyhydroxylated

fullerene $C_{60}(OH)_{36}$ (**2**) was prepared by a previously reported method using hydrogen peroxide and nanom spectra D100 as starting materials.[66-70]

**2.3. Sorption measurements.** The adsorption/desorption isotherms for $H_2O$ at 298 K, MeOH at 288 K, and EtOH at 298 K were measured with a BELSORP-aqua automatic volumetric adsorption apparatus (BEL Japan, Inc.). The $N_2$, $CO_2$, $H_2$, and $CH_4$ adsorption/desorption isotherms were measured with BELSORP-max and BELSORP-mini automatic volumetric adsorption apparatuses (BEL Japan, Inc.) at 77, 195 (and 298 K), 77, and 173 K, respectively. The high-pressure $CO_2$ adsorption and desorption isotherms were measured using a BELSORP-HP volumetric adsorption instrument (BEL Japan, Inc.). Before the measurements, **1**•x($H_2O$) and **2**•x($H_2O$) were heated at 373-380 K under a reduced pressure ($<10^{-2}$ Pa) to remove the $H_2O$ molecules.

## 3. Results and Discussion

**3.1. Thermal property and molecular-assembly.** The hydroxyl-functionalized hydrophilic surfaces of **1** and **2** can effectively form the intermolecular hydrogen-bonding network. As-grown amorphous **1** and **2** were obtained as the hydrated species of **1**•x($H_2O$) and **2**•x($H_2O$), where x depends on the humidity. TG analyses show a gradual dehydration process from room temperature accompanying the gradual weight-loss. The weight-loss percentages of **1**•x($H_2O$) and **2**•x($H_2O$) at 400 K are approximately 10.6 and 16.2%, respectively (Figure S1), which correspond to calculated weights of 10.5% for **1**•6($H_2O$) and of 16.8% for **2**•15($H_2O$), respectively. Therefore, the typical formulas of amorphous **1** and **2** at approximately 40% relative humidity are **1**•6($H_2O$) and **2**•15($H_2O$), respectively. After the dehydration, next weight loss corresponding to the thermal decomposition starts at ca. 460 K for **1**, while **2** starts to decompose just after the dehydration, that is, at ca. 400 K, suggesting that the hydrogen-bonding network in **1** is more thermally stable.

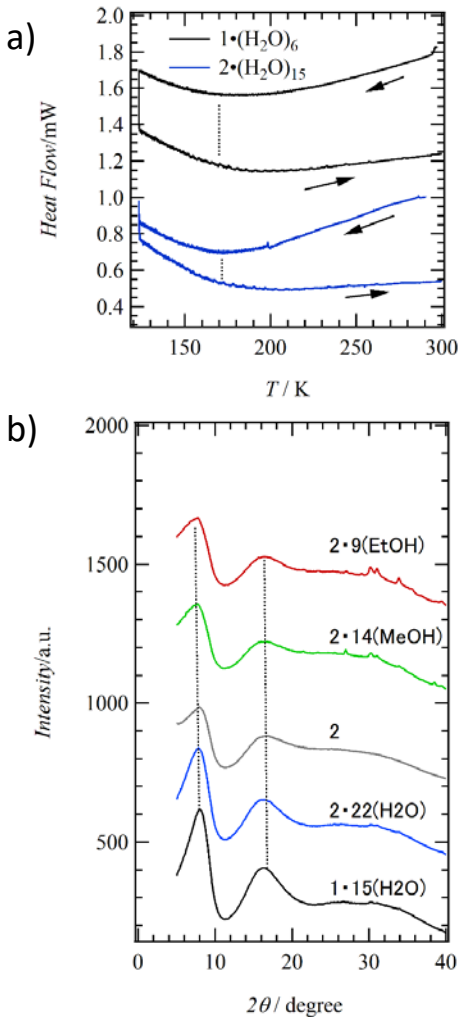


**Figure 1.** Phase transition and molecular assembly structures of solid-state **1** and **2**. a) DSC diagrams of **1**•6($H_2O$) and **2**•15($H_2O$). b) PXRD patterns of **1**•15($H_2O$) (black pattern), **2**•22($H_2O$) (blue pattern), **2** (gray pattern), **2**•14(MeOH) (green pattern), and **2**•9(EtOH) (red pattern) at 298 K.

Figure 1a shows DSC diagrams of **1**•6($H_2O$) and **2**•15($H_2O$) from 120 to 300 K. Although the first-order phase transition from liquid to solid water is not observed around 273 K in the cooling process, the baseline anomaly around 170 K is associated with the thermally activated solid-glass transition of thermally fluctuated polar $H_2O$ molecules. Figure 1b summarizes the PXRD patterns of **1**•15($H_2O$), **2**•22($H_2O$), **2** at 298 K, indicating the low crystallinity and amorphous state for all molecular assemblies. The broad diffraction peaks at $2\theta = 9.40°$ and 18.7° for **1**•15($H_2O$) are assigned to the short-range order

of $d \approx 0.94$ and $d \approx 0.47$ nm, respectively, whereas those at $2\theta = 7.88°$ and 16.3° for **2**•22($H_2O$)$_{22}$ correspond to $d \approx 1.12$ and $d \approx 0.54$ nm, respectively. Amorphous-like molecular assembly structures of **1**•6($H_2O$) and **2**•15($H_2O$) are consistent with the glass transition behavior of $H_2O$ around 170 K in the DSC diagrams. The short-range periodicities of $d \approx 0.94$ and $d \approx 1.12$ nm are almost consistent with the average diameters of $C_{60}(OH)_{12}$ and $C_{60}(OH)_{36}$, respectively, whereby decreasing the number of –OH groups from x = 36 to x = 12 reduces the average diameter. The removal of $H_2O$ from (**2**)•15($H_2O$) slightly changes the PXRD pattern with a broad diffraction peak around $2\theta = 7.96°$ with $d \approx 1.1$ nm, which is the same as that for **2**•22($H_2O$).

**3.2. $H_2O$ dynamics in solids**. Changes in the DSC baselines of **1**•6($H_2O$) and **2**•15($H_2O$) around 170 K are associated with the glass transition of thermally activated $H_2O$ molecules within the pores of O-H•••O hydrogen-bonding networks of amorphous **1** and **2**. The dielectric spectra are sensitive to the molecular motion of polar structural units in the measuring frequency range from 1 kHz to 1 MHz.[75] When the frequency of the molecular motion is close to that of the measuring frequency, a Debye-type dielectric relaxation is observed in the dielectric measurements. Figure 2 summarizes the real part ($\varepsilon_1$) and imaginary part ($\varepsilon_2$) of the dielectric constants of **1**•6($H_2O$) and **2**•15($H_2O$), together with dehydrated **1** and **2** on the compressed pellets. Both of the $\varepsilon_1$ and $\varepsilon_2$ values are largely enhanced by increasing the temperature and decreasing the frequency above ~200 K. The values of $\varepsilon_1 = 460$ and $\varepsilon_2 = 340$ for **1**•6($H_2O$) at 280 K are approximately one hundred times larger than that at 150 K and 1 kHz, suggesting that the molecular motion of the polar structural unit is thermally activated by increasing the temperature above 200 K. The baseline anomaly in the DSC measurements were observed around 170 K, where the molecular motion of $H_2O$ molecules was just thermally activated by increasing in the temperature. On the contrary, the collective motion of the polar hydrogen-bonding network was observed in the frequency-dependent dielectric enhancements. Such dynamic molecular motions have been observed in the huge dielectric responses in organic–inorganic perovskite crystals.[76, 77] The thermally activated molecular motion of the polar $H_2O$ molecules mainly contributes to the dielectric enhancements in the measuring

frequency range because the magnitude of $\varepsilon_1$ = 480 for **1**•6($H_2O$) is six times larger than that of $\varepsilon_1$ = 85 for dehydrated **1** at 280 K. The large value of $\varepsilon_2 \approx 300$ strongly supports the highly protonic conductive behavior of **1**•6($H_2O$) around 280 K.

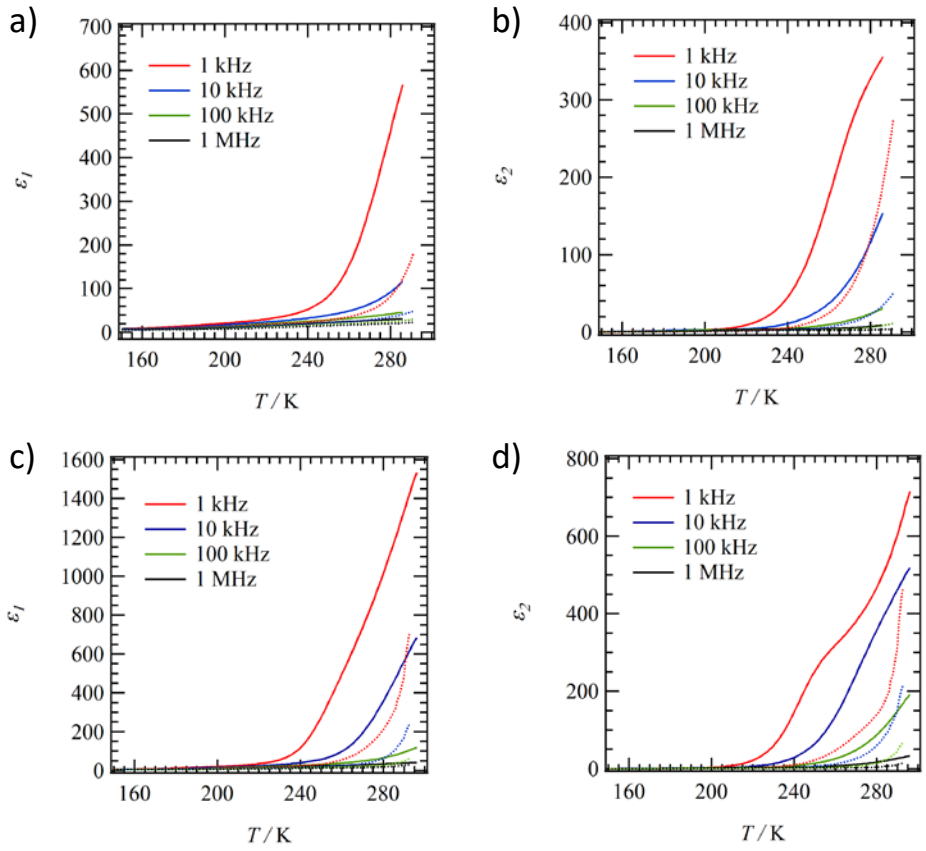


**Figure 2.** Temperature- and frequency-dependent real ($\varepsilon_1$) and imaginary ($\varepsilon_2$) parts of the dielectric constants for a, b) **1**•6($H_2O$) (solid lines) and dehydrated **1** (dashed lines), and c, d) **2**•15($H_2O$) (solid lines) and dehydrated **2** (dashed lines) during cooling from 285 K.

Similar dielectric enhancements are clearly observed for **2**•16($H_2O$). The $\varepsilon_1$ and $\varepsilon_2$ values of **2**•$(H_2O)_{16}$ at 280 K are approximately two hundred times larger than those at 150 K with a frequency, $f$ = 1 kHz, and the dielectric constants and dielectric enhancements of **2**•16($H_2O$) are much larger than those of **1**•6($H_2O$)

because of the larger amount of –OH groups and $H_2O$ molecules. A Debye-type dielectric relaxation was observed in the dielectric measurements of **2**•16($H_2O$). The frequency-dependent conductance (*G*) and susceptance (B) spectra and its Cole-Cole plots indicated a typical semicicular trance at 300 K (Figure S7). A relation time ($\tau$) of the dipole motion of hydrogen-bonding $H_2O$ molecules was estimated as $2.58\times10^{-4}$ sec at 300 K. Relatively high proton conductivity of hydrated **2**•16($H_2O$) was observed at $2.8\times10^{-4}$ $Scm^{-1}$ at 300 K due to the existence of hydrogen-bonding network and acidic –OH group to generate the protonic carrier. The complete $H_2O$ removal from **2**•16($H_2O$) decreases the $\varepsilon_1$ value from 1050 to 210 at 1 kHz, which is consistent with the dielectric anomaly for the thermally activated molecular motion of polar $H_2O$ in amorphous state **1** and **2**. A broad anomaly for the $\varepsilon_2$ value is observed in **2**•16($H_2O$) around 255 K because of the motional freedom of $H_2O$ and a relatively large $\varepsilon_2$ value of 500 at 280 K, indicating the proton conducting property of **2**•16($H_2O$). The dielectric spectra of **1**•6($H_2O$) and **2**•15($H_2O$) are consistent with the glass transition of polar $H_2O$ molecules around 170~220 K within the hydrogen-bonding networks of amorphous **1** and **2**. Much larger $\varepsilon_1$ and $\varepsilon_2$ values of **2**•x($H_2O$) than those of **1**•x($H_2O$) corresponded to larger magnitude of motional freedom of hydrogen-bonding networks of **2**. The $H_2O$ dependent dielectric responses of crystals **2**•x($H_2O$) were evaluated in vacuum and fully saturated $H_2O$ condition, respectively, using the compressed pellets (Figure S10). The dehydrated **2** indicated simple dielectric enhancements at low frequency and high temperature condition due to the thermally activated fluctuation of the hydrogen-bonding $C_{60}(OH)_{36}$ network by increasing in the temperature up to 300 K. On the contrary, the hydrated **2**•16($H_2O$) under the saturated $H_2O$ condition indicated huge dielectric enhancements and also discontinuous $\varepsilon_1$- and $\varepsilon_2$-changes around solid–liquid phase transition temperature of bulk $H_2O$ around 273 K. Therefore, sufficient amount of $H_2O$ molecules in hydrogen-bonding $C_{60}(OH)_{36}$ hydrogen-bonding network formed the bulk environment of $H_2O$ hydrogen-bonding network.[78] However, the $H_2O$ adsorption-desorption isotherm at 298K clearly indicated the unstable liquid state $H_2O$ sorption state in the hydrogen-bonding $C_{60}(OH)_{36}$ network. Under

the saturated $H_2O$ condition, the $H_2O$ molecules could be stably existed in the hydrogen-bonding $C_{60}(OH)_{36}$ network accompanying with dielectric anomaly around 273 K.

**3.3. Gas and vapor sorption properties**. To elucidate a porosity, gas and vapor adsorption/desorption isotherms were measured. Table 1 summarizes the adsorption-desorption parameters of amorphous **1** and **2**. Figure 3a shows the $N_2$ adsorption-desorption isotherms of amorphous **1** and **2** at 77 K. The $N_2$ adsorption amounts for **1** and **2** are about 2 and 28 mol $mol^{-1}$, respectively, at $P/P_0$~1. The abrupt adsorption increase for amorphous **2** from $n_{ads} \approx 12$ to ~28 at $P/P_0 \approx 0.92$ may be $N_2$ adsorption at the macropores of the powdered sample. Therefore, approximately twelve $N_2$ molecules are adsorbed into the nanopores of amorphous **2**, providing **2**•$(N_2)_{12}$. **1** has the type-I isotherm typical for nanoporous materials, while the isotherms of **2** shows gradual uptake with a hysteresis. On the other hand, the $CO_2$ adsorption-desorption isotherms at 195 K are the type-I with almost no hysteresis. The I-type $CO_2$ sorption isotherm suggests the existence of nanopores in amorphous **1** and **2**. The presence of nanopores in amorphous **1** and **2** was also confirmed from the $H_2$ adsorption measurements, in which both compounds reversibly adsorb $H_2$ at 77 K, resulting in the chemical formulas of **1**•2.5$(H_2)$ and **2**•4$(H_2)$, as shown in Figure 3c). The BET specific surface area calculated from the $CO_2$ adsorption data are 312 and 333 $m^2\ g^{-1}$ for amorphous **1** and **2**, respectively. Two kinds of amorphous-like LMW organic sorption materials were reported by Atwood et al.[58] The first compound of noria has an intrinsic cage within the molecule, which showed a high $CO_2$ selectivity for gas adsorption with a BET specific surface area of 40 $m^2\ g^{-1}$ from the $N_2$ adsorption-desorption isotherm at 77 K. The second amorphous compound was reported in the intrinsic cage-type cucurbit[7]uril molecule,[58] indicating higher $CO_2$ adsorption behavior than those for $N_2$ and $CH_4$. The BET specific surface area of the latter compound is much smaller than those of **1** and **2**. The three-dimensional extrinsic pores of the hydrogen-bonding networks for amorphous **1** and **2** are useful for repeated adsorption-desorption cycles. From the liquid density of $N_2$ ($d$ = 0.808 g $cm^{-3}$) and the solid density of $CO_2$ ($d$ = 1.56 g $cm^{-3}$), the occupied volumes of $N_2$ ($n_{max}$ = 5.35) and $CO_2$ ($n_{max}$ = 12.0) for amorphous **2** are approximately 0.368 and 0.115 $cm^3\ g^{-1}$, respectively. On the contrary, the occupied volumes of the $N_2$ ($n_{max}$ = 2.34) and $CO_2$ ($n_{max}$ = 3.17) for amorphous **1** are approximately

0.089 and 0.098 $cm^3 g^{-1}$, respectively. **2** has similar occupied volumes for both gases, while the occupied volume of **2** for $N_2$ was larger than that for $CO_2$, which may be due to the structural expansion of hydrogen-bonding framework. The $CH_4$ adsorption/desorption isotherms also showed similar trend to $N_2$: only **2** has large hysteresis as shown in Figure 3d). It is worth noting that more hydrophobic $N_2$ and $CH_4$ than $CO_2$ induced the structural changes. All gas sorption results imply that the balance of hydrophobicity/hydrophilicity in the hydrogen-bonding networks and gas molecules determines the sorption behaviors.

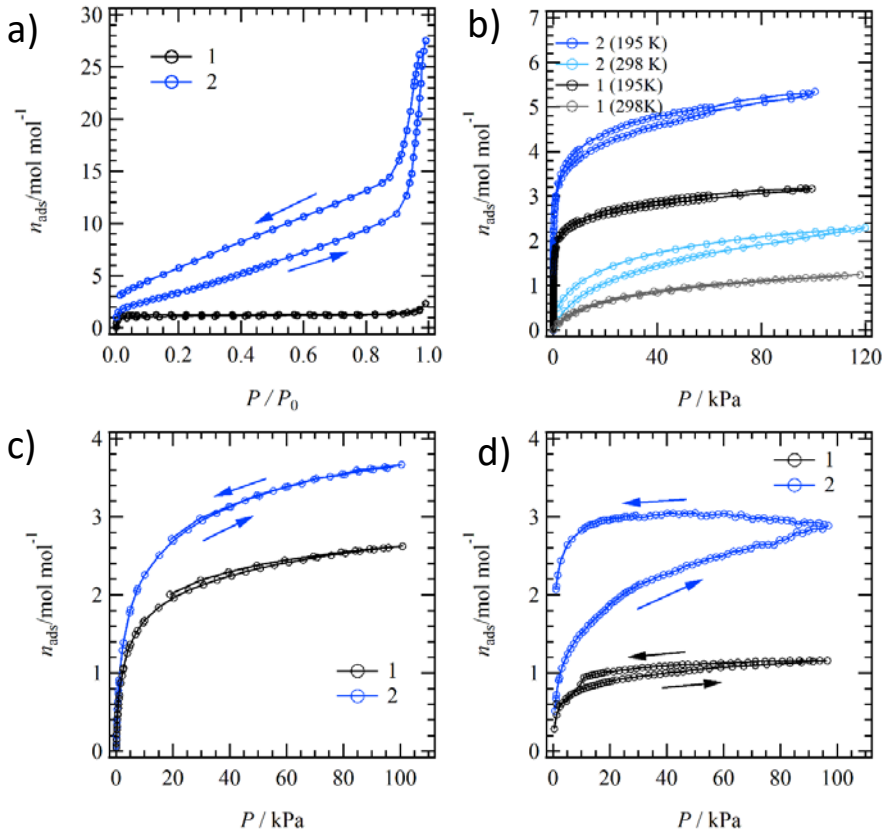


**Figure 3**. Gas adsorption-desorption properties of **1** and **2**. a) $N_2$ adsorption-desorption isotherm at 77 K. b) $CO_2$ adsorption-desorption isotherm at 195 and 298 K. c) $H_2$ adsorption-desorption isotherm at 77 K. d) $CH_4$ adsorption-desorption isotherm at 173 K.

It is expected that the surface-modified -OH groups on $C_{60}(OH)_x$ play an important role not only for the formation of hydrogen-bonding network pores but also for the adsorption sites for gas molecules. To evaluate the strength of the interaction between the hydrogen-bonding networks and $CO_2$ molecules, the enthalpy of $CO_2$ adsorption ($Q_{st}$) was calculated. First, the dual-site Langmuir−Freundlich equation (eq. 1) was employed to model the $CO_2$ adsorption isotherms at 278, 288, and 298 K for amorphous **1** and **2** (Figure S8).[79]

$$q = \frac{q_{sat,A} b_A P^{\alpha_A}}{1+b_A P^{\alpha_A}} + \frac{q_{sat,B} b_B P^{\alpha_B}}{1+b_B P^{\alpha_B}} \quad (1)$$

here, $q$ is the amount of adsorbed $CO_2$ (mmol $g^{-1}$), $p$ is the pressure (bar), $q_{sat}$ is the saturation capacity (mmol $g^{-1}$), $b$ is the Langmuir−Freundlich parameter ($bar^{-\alpha}$), and $\alpha$ is the Langmuir−Freundlich exponent (dimensionless) for adsorption sites A and B. The Clausius−Clapeyron equation (eq. 2) was then used to calculate $Q_{st}$ by determining the slope of the best-fit line for ln $p$ versus $1/T$ at each loading.

$$(lnp)_q = \left(\frac{Q_{ST}}{R}\right)\left(\frac{1}{T}\right) + C \quad (2)$$

The magnitudes of $Q_{st}$ for $CO_2$ adsorption of amorphous **1** and **2** are –46 and –42 kJ $mol^{-1}$ at zero coverage, respectively (Figure 4a). There is no significant difference for the $Q_{st}$ values of amorphous **1** and **2** with different numbers of -OH groups, and increasing $q$ values gradually decrease the absolute value of $Q_{st}$. Since the $Q_{st}$ values of amorphous **1** and **2** are comparable to that of zeolite ($Q_{st}$ = –49.1 and –50.0 for NaX and Na-ZSM-5, respectively),[80] the hydrogen-bonding network structure of the –OH groups should act as hydrophilic gas adsorption sites. Temperature-dependent in situ vibrational spectra of amorphous **2** were measured (Figure 4b) to evaluate the intermolecular interaction at the –OH hydrogen-bonding network sites.

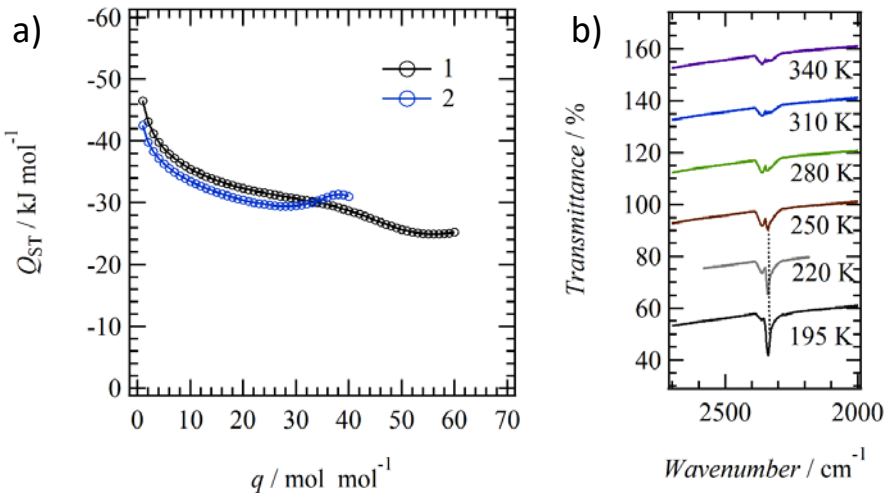


**Figure 4.** $CO_2$ adsorption of **2**. a) Enthalpy of $CO_2$ adsorption ($Q_{st}$) as a function of loading. b) Temperature-dependent in situ vibration spectra of the antisymmetric C=O stretching band ($\nu^a_{CO2}$) under a $CO_2$ environment.

At 195 K, the antisymmetric C=O stretching mode of $CO_2$ ($\nu^a_{CO2}$) is observed at 2338 cm$^{-1}$, and its intensity gradually decreases as the temperature increases. The $\nu^a_{CO2}$ band for gas-phase $CO_2$ molecules is observed at 2349 cm$^{-1}$. Therefore, the $\nu^a_{CO2}$ band of amorphous **2** is red-shifted by approximately 10 cm$^{-1}$ under a $CO_2$ environment. The physical $CO_2$ adsorption in various host materials appears as the $\nu^a_{CO2}$ band from 2328 to 2368 cm$^{-1}$;[81] thus, the $CO_2$ molecules in amorphous **2** are physically adsorbed into the pores of the O-H•••O hydrogen-bonding network. Adsorption of $CO_2$ molecules at Lewis acidic and Lewis basic sites result in a blue-shift and red-shift of the $\nu^a_{CO2}$ bands, respectively.[82-84] The red-shifted $\nu^a_{CO2}$ band under a $CO_2$ environment of amorphous **2** indicates the interaction between the carbon atom of $CO_2$ and the oxygen atom of the –OH sites. Increasing the temperature gradually released $CO_2$ gas from the hydrogen-bonding network pores of amorphous **2**, decreasing the intensity of the $\nu^a_{CO2}$ band.

**Table 1. Sorption properties of 1 and 2.**

| | | **1** | | | | **2** | | | |
|---|---|---|---|---|---|---|---|---|---|
| Adsorbate | $T$ K | $P/P_0$ | $P$ kPa | $n_{max}$ mol mol$^{-1}$ | $n_{max}$ cm$^3$(STP) g$^{-1}$ | $P/P_0$ | $P_0$ kPa | $n_{max}$ mol mol$^{-1}$ | $n_{max}$ cm$^3$(STP) g$^{-1}$ |
| $H_2O$ | 298 | 0.95 | – | 8.87 | 212 | 0.95 | – | 21.8 | 370 |
| MeOH | 288 | 0.98 | – | 7.36 | 178 | 0.96 | – | 13.8 | 235 |
| EtOH | 298 | 0.97 | – | 5.07 | 123 | 0.96 | – | 9.23 | 157 |
| $N_2$ | 77 | 0.99 | – | 2.34 | 57.4 | 0.99 | – | 12.0 (27.5)[a] | 238 (469)[a] |
| $CO_2$ | 195 | 0.98 | – | 3.17 | 77.9 | 0.99 | – | 5.35 | 91.1 |
| $CO_2$ | 298 | – | 118 | 1.24 | 30.1 | – | 120 | 2.30 | 38.6 |
| $H_2$ | 77 | – | 101 | 2.62 | 64.5 | – | 100 | 3.67 | 61.7 |
| $CH_4$ | 173 | – | 96.6 | 1.16 | 28.5 | – | 95.4 | 2.90 | 48.6 |

[a] $n_{max}$ in parentheses includes the adsorption for the macropores of the powdered sample.

Table 1 summarizes the adsorption-desorption parameters of amorphous **1** and **2** for $H_2O$ ($T$ = 298 K), MeOH ($T$ = 288 K), and EtOH ($T$ = 298 K). Before the adsorption measurements, the solids were kept at 373 K under vacuum ($10^{-2}$ Pa) for 18 h to completely remove $H_2O$ molecules. The adsorption-desorption isotherms of amorphous **1** and **2** for $H_2O$ indicate reversible adsorption-desorption behavior (Figure 5 and Figure S2), where the maximum adsorption amounts ($n_{max}$) of **1** and **2** are 10 and 22, respectively, at $P/P_0 \approx 0.95$. Similarly, reversible adsorption-desorption behaviors for MeOH ($T$ =288 K) and EtOH ($T$ = 298 K) are observed in amorphous **1** and **2**. The $n_{max}$ values of amorphous **1** and **2** for MeOH are approximately 7 and 14, respectively, whereas those for EtOH are 5 and 9, respectively (Figure S2). The magnitude of $n_{max}$ for amorphous **2** is approximately twice that of **1** because **2** has more -OH groups per one fullerene unit. From the liquid densities of $H_2O$ ($d_{293K}$ = 0.998 g cm$^{-3}$), MeOH ($d_{293K}$ = 0.793 g cm$^{-3}$), and EtOH ($d_{293K}$ = 0.789 g cm$^{-3}$), the occupied volumes of the guest $H_2O$ (n = 21.8), MeOH (n = 13.8),

and EtOH (n = 9.23) molecules for amorphous **2** are approximately 0.298, 0.423, and 0.409 $cm^3\ g^{-1}$, respectively. On the contrary, the occupied volumes of the guest $H_2O$ (n = 8.87), MeOH (n = 7.36), and EtOH (n = 5.07) molecules for amorphous **1** are approximately 0.171, 0.321, and 0.320 $cm^3\ g^{-1}$, respectively. These values are considerably larger than those calculated form the $CO_2$ adsorption data. In addition, all vapor adsorption/desorption isotherms showed hysteresis. These results suggest that the molecules with hydroxyl groups induce the structural changes. Hydrophilic pores decorated by OH groups contribute to high adsorption amounts for polar $H_2O$, $CH_3OH$, and $C_2H_5OH$ molecules. The similar occupied volumes of **1** and **2** for MeOH and EtOH suggested the similar porosity for the adsorption states. However, the occupied volumes of **1** and **2** for $H_2O$ are considerably smaller than those for MeOH and EtOH, indicating a different porosity and adsorption environment around –OH groups. The guest polar molecules, such as $H_2O$, MeOH, and EtOH can be captured in the intermolecular O-H•••O hydrogen-bonding networks between the surface-modified –OH groups on $C_{60}$, where the interaction mode of $H_2O$ is different from those of MeOH and EtOH.

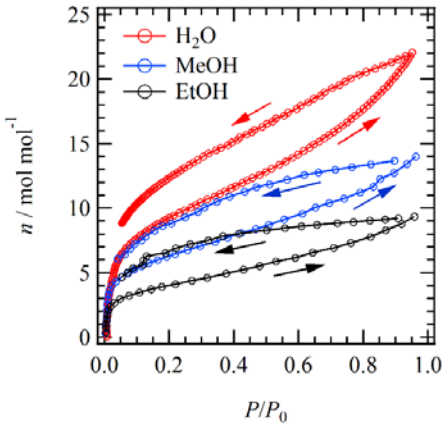


**Figure 5**. Adsorption-desorption isotherms of **2** for $H_2O$ at 298 K (red), MeOH at 288 K (blue), and EtOH at 298 K (black).

## 4. Conclusion

Two kinds of –OH-modified $C_{60}$ derivatives of $C_{60}(OH)_{12}$ (**1**) and $C_{60}(OH)_{36}$ (**2**) showed reversible vapor ($H_2O$, MeOH, and EtOH) and gas ($N_2$, $CO_2$, $H_2$, and $CH_4$) adsorption-desorption behaviors at the O-H•••O hydrogen-bonding network pores of the amorphous molecular assemblies. The maximum $H_2O$ adsorption amounts were (**1**)•15($H_2O$) and (**2**)•22($H_2O$), respectively, at $P/P_0$~0.95 with $T$ = 298 K. The surface-modified –OH groups formed hydrogen-bonding hydrophilic network pores to adsorb polar $H_2O$ molecules, which thermally activated dynamics was confirmed in the dielectric enhancement in the low frequency and protonic conductivity. The larger hydrophilic surface of **2** than that of **1** provided relatively high adsorption abilities for the polar molecules. Three-dimensional O-H•••O hydrogen-bonding network pores of surface-modified –OH groups of **1** and **2** formed the hydrophilic extrinsic Lewis acidic network pores, where the reversible adsorption-desorption behaviors were observed for $N_2$, $CO_2$, $H_2$, and $CH_4$ gases. The BET specific surface areas of amorphous **1** and **2** were 312 and 335 $m^2\ g^{-1}$, respectively, from the $CO_2$ adsorption isotherms at 195 K. Hydroxyl-functionalized $C_{60}$ derivatives can form the extrinsic hydrogen-bonding network pores to control the dielectric constants, which became the first gas sorption LMW amorphous organic materials with extrinsic O-H•••O network pores.

**ASSOCIATED CONTENT**

**Supporting Information**. TG charts, adsorption-desorption isotherm of **1** for $H_2O$ at 298 K, $CH_3OH$ at 288 K, $C_2H_5OH$ at 298 K, temperature dependent PXRD patterns of **1**•6($H_2O$) and **2**•15($H_2O$), proton conducting property of **2**•16($H_2O$), high pressure $CO_2$ adsorption-desorption isotherm of **2** at 278, 288, and 298 K, $H_2O$ dependent dielectric responses of crystals **2**•n($H_2O$), and IR spectra. This material is available free of charge via the Internet at http://pubs.acs.org.

## AUTHOR INFORMATION

Corresponding Author

* akutagawa@tohoku.ac.jp and noro@ess.hokudai.ac.jp

### Notes

The authors declare no competing financial interest.

## ACKNOWLEDGMENTS

This work was supported by a Grant-in-Aid for Scientific Research on Innovative Areas Kiban Kenkyu (A) (JP19H00886), Japan Science and Technology Agency CREST Grant Number JPMJCR18I4, and 'Dynamic Alliance for Open Innovation Bridging Human, Environment and Materials' from the Ministry of Education, Culture, Sports, Science and Technology.

## References

(1) Davis, M. E. Ordered Porous Materials for Emerging Applications. *Nature* **2002**, *417*, 813–821.

(2) Ma, Y.; Tong, W.; Zhou, H.; Sui, S. L. A Review of Zeolite-Like Porous Materials. *Microporous Mesoporous Mater*. **2000**, *37*, 243–252.

(3) McKeown, N. B.; Budd, P. M. Polymers of Intrinsic Microporosity (PIMs): Organic Materials for Membrane Separations, Heterogeneous Catalysis and Hydrogen Storage. *Chem. Soc. Rev*. **2006**, *35*, 675–683.

(4) Morris, R. E.; Wheatley, P. S. Gas Storage in Nanoporous Materials. *Angew. Chem., Int. Ed*. **2008**, *47*, 4966–4981.

(5) Zhou, H.-C.; Long, J. R.; Yaghi, O. M. Introduction to Metal–Organic Frameworks. *Chem. Rev*., **2012**, *112*, 673–674.

(6) Kitagawa, S.; Kitaura, R.; Noro, S. Functional Porous Coordination Polymers. *Angew. Chem., Int. Ed*. **2004**, *43*, 2334–2375.

(7) Côte, A. P.; Benin, A. I.; Ockwig, N. W.; O'Keeffe, M.; Matzger, A. J.; Yaghi, O. M. Porous, Crystalline, Covalent Organic Frameworks. *Science* **2005**, *310*, 1166–1170.

(8) Ding, S.-Y.; Wang, W. W. Covalent Organic Frameworks (COFs): From Design to Applications. *Chem. Soc. Rev*. **2013**, *42*, 548–568.

(9) Feng, X.; Dinga, X.; Donglin, J. Covalent Organic Frameworks. *Chem. Soc. Rev*. **2012**, *41*, 6010–6022.

(10) Makiura, R.; Motoyama, S.; Umemura, Y.; Yamanaka, H.; Sakata, O.; Kitagawa, K. Surface Nano-Architecture of A Metal-Organic Framework. *Nat. Mater.* **2010**, *9*, 565–571.

(11) Shekhah, O.; Liu, J.; Fischer, R. A.; Wöll, C. MOF Thin Films: Existing and Future Applications. *Chem. Soc. Rev*. **2011**, *40*, 1081–1161.

(12) Kung, C.-W.; Wang, T. C.; Mondloch, J. E.; Fairen-Jimenez, D.; Gardner, D. M.; Bury, W.; Klingsporn, J. M.; Barnes, J. C.; Duyne, R. V.; Stoddart, J. F.; Wasielewski, M. R.; Farha, O, K.; Hupp, J. T. Metal–Organic–Framework Thin Films Composed of Free-Standing Acicular Nanorods Exhibiting Reversible Electrochromism. *Chem. Mater*. **2013**, *25*, 5012−5017.

(13) Pfeffermann, M.; Dong, R,; Graf, R.; Zajaczkowski, W.; Gorelik, T.; Pisula, W.; Narita, A.; Müllen, K.; Feng, X. Free-Standing Monolayer Two-Dimensional Supramolecular Organic Framework with Good Internal Order. *J. Am. Chem. Soc*. **2015**, *137*, 14525–14532.

(14) Tian, J.; Chen, L.; Zhang, D.-W.; Liu, Y.; Li, Z.-T. Supramolecular Organic Frameworks: Engineering Periodicity in Water Through Host–Guest Chemistry. *Chem. Commun*. **2016**, *52*, 6351–6362.

(15) Mastalerz, M. Permanent Porous Materials from Discrete Organic Molecules−Towards Ultra‐High Surface Areas. *Chem. - Eur. J*. **2012**, *18*, 10082–10091.

(16) Tian, J.; Thallapally, P. K.; McGrail, B. P. Porous Organic Molecular Materials. *CrystEngComm* **2012**, *14*, 1909–1919.

(17) Holst, J. R.; Trewin, A.; Cooper, A. I. Porous Organic Molecules. *Nat. Chem*. **2010**, *2*, 915–920.

(18) Atwood, J. L.; Barbour, L. J.; Jerga, A. Storage of Methane and Freon by Interstitial van der Waals Confinement. *Science* **2002**, *296*, 2367–2369.

(19) Atwood, J. L.; Barbour, L. J.; Jerga, A.; Schottel, B. L. Guest Transport in A Nonporous Organic Solid via Dynamic van der Waals Cooperativity. *Science* **2002**, *298*, 1000–1002.

(20) Tsue, H.; Takahashi, H.; Ishibashi, K.; Inoue, R.; Shimizu, S.; Takahashi, D.; Tamura, R. Crystallographic Analysis of $CO_2$ Sorption State in Seemingly Nonporous Molecular Crystal of Azacalix[4]arene Tetramethyl Ether Exhibiting Highly Selective $CO_2$ Uptake. *CrystEngComm* **2012**, *14*, 1021-1026.

(21) Enright, G. D.; Udachin, K. A.; Moudrakovski, I. L.; Ripmeest, J. A. Thermally Programmable Gas Storage and Release in Single Crystals of An Organic van der Waals Host. *J. Am. Chem. Soc*. **2003**, *125*, 9896–9897.

(22) Herbert, S. A.; Janiak, A.; Thallapally, P. K.; Atwood, J. L.; Barbour, L. J. Diffusion of Vaporous Guests into A Seemingly Non-Porous Organic Crystal. *Chem. Commun*. **2014**, *50*, 15509–15512.

(23) Patil, R. S.; Banerjee, D.; Zhang, C.; Thallapally, P. K.; Atwood, J. L. Selective $CO_2$ Adsorption in A Supramolecular Organic Framework. *Angew. Chem., Int. Ed*. **2016**, *55*, 4523–4526.

(24) Jiang, S.; Jones, J. T. A.; Trewin, A.; Hasell, T.; Cooper, A. I. Porous Organic Molecular Solids by Dynamic Covalent Scrambling. *Nat. Commun*. **2011**, *2*, 207–1–4.

(25) Jones, J. T. A.; Hasell, T.; Wu, X.; Bacsa, J.; Jelfs, K. E.; Schmidtmann, M.; Chong, S. Y.; Adams, D. J.; Trewin, A.; Schiffman, F.; Cora, F.; Slater, B.; Steiner, A.; Day, G. M.; Cooper, A. I. Modular and Predictable Assembly of Porous Organic Molecular Crystals. *Nature* **2011**, *474*, 367–371.

(26) Jiang, S.; Bacsa, J.; Wu, X.; Jones, J. T. A.; Dawson, R.; Trewin, A.; Adams, D. J.; Cooper, A. I. Selective Gas Sorption in A [2+3] 'Propeller' Cage Crystal. *Chem. Commun*. **2011**, *47*, 8919–8921.

(27) Mitra, T.; Wu, X.; Clowes, R.; Jones, J. T. A.; Jelfs, K. E.; Adams, D. J.; Trewin, A.; Bacsa, J.; Steiner, A.; Cooper, A. I. A Soft Porous Organic Cage Crystal with Complex Gas Sorption Behavior. *Chem. - Eur. J*. **2011**, *17*, 10235–10240.

(28) Schneider, M. W.; Oppel, I. M.; Ott, H.; Lechner, L. G.; Hauswald, H. J.; Stoll, R.; Mastalerz, M. Periphery-Substituted [4+6] Salicylbisimine Cage Compounds with Exceptionally High Surface Areas: Influence of the Molecular Structure on Nitrogen Sorption Properties. *Chem. - Eur. J*. **2012**, *18*, 836–847.

(29) Hasell, T.; Chong, S. Y.; Jelfs, K. E.; Adams, D. A.; Cooper, A. I. Porous Organic Cage Nanocrystals by Solution Mixing. *J. Am. Chem. Soc*. **2012**, *134*, 588–598.

(30) Kim, H.; Kim, Y.; Yoon, M.; Lim, S.; Park, S. M.; Seo, G.; Kim, K. Highly Selective Carbon Dioxide Sorption in An Organic Molecular Porous Material. *J. Am. Chem. Soc*. **2010**, *132*, 12200–12202.

(31) Tian, J.; Ma, S.; Thallapally, P. K.; Fowler, D.; McGrail, B. P.; Atwood, J. L. Cucurbit[7]uril: An Amorphous Molecular Material for Highly Selective Carbon Dioxide Uptake. *Chem. Commun*. **2011**, 47, 7626–7628.

(32) Soldatov, D. V.; Moudrakovski, I. L.; Ripmeester, J. A. Dipeptides as Microporous Materials. *Angew. Chem., Int. Ed*. **2004**, *43*, 6308–6311.

(33) Praveen K.; Thallapally, B. P. M.; Atwood, J. L.; Gaeta, C.; Tedesco, C.; Neri, P. Carbon Dioxide Capture in a Self-Assembled Organic Nanochannels. *Chem. Mater*. **2007**, *19*, 3355–3357.

(34) Afonso, R. V.; Durão, J.; Mendes, J. A.; Damas, A. M.; Gales, L. Dipeptide Crystals As Excellent Permselective Materials: Sequential Exclusion of Argon, Nitrogen, and Oxygen. *Angew. Chem., Int. Ed*. **2010**, *49*, 3034–3036.

(35) Jin, Y.; Voss, B. A.; Jin, A.; Long, H.; Noble, R. D.; Zhang, W. Highly $CO_2$-Selective Organic Molecular Cages: What Determines the $CO_2$ Selectivity. *J. Am. Chem. Soc*. **2011**, *133*, 6650–6658.

(36) He, Y.; Xiang, S.; Chen, B. A Microporous Hydrogen-Bonded Organic Framework for Highly Selective $C_2H_2/C_2H_4$ Separation at Ambient Temperature. *J. Am. Chem. Soc*. **2011**, *133*, 14570–14573.

(37) Mastalerz, M.; Schneider, M. W.; Oppel, I. M.; Presly, O. A Salicylbisimine Cage Compound with High Surface Area and Selective $CO_2/CH_4$ Adsorption. *Angew. Chem., Int. Ed*. **2011**, *50*, 1046–1051.

(38) Schneider, M. W.; Oppel, I. M.; Mastalerz, M. Exo‐Functionalized Shape‐Persistent [2+3] Cage Compounds: Influence of Molecular Rigidity on Formation and Permanent Porosity. *Chem. - Eur. J*. **2012**, *18*, 4156–4160.

(39) Yamamoto, A.; Hamada, T.; Hisaki, I.; Miyata, M.; Tohnai, N. Dynamically Deformable Cube-Like Hydrogen-Bonding Networks in Water-Responsive Diamondoid Porous Organic Salts. *Angew. Chem., Int. Ed*. **2013**, *52*, 1709–1712.

(40) Sozzani, P.; Comotti, A.; Bracco, S.; Simonutti, R. A Family of Supramolecular Frameworks of Polyconjugated Molecules Hosted in Aromatic Nanochannels. *Angew. Chem. Int. Ed*. **2004**, *43*, 2792–2797.

(41) Sozzani, P.; Bracco, S.; Comotti, A.; Ferretti, L.; Simonutti, R. Methane and Carbon Dioxide Storage in A Porous van der Waals Crystal. *Angew. Chem., Int. Ed*. **2005**, *44*, 1816–1820.

(42) Msayib, K. J.; Book, D.; Budd, P. M.; Chaukura, N.; Harris, K. D. M.; Helliwell, M.; Tedds, S.; Walton, A.; Warren, J. E.; Xu, M.; McKeown, N. B. Nitrogen and Hydrogen Adsorption by An Organic Microporous Crystal. *Angew. Chem., Int. Ed*. **2009**, *48*, 3273–3277.

(43) Mastalerz, M.; Oppel, I. R. Rational Construction of An Extrinsic Porous Molecular Crystal with An Extraordinary High Specific Surface Area. *Angew. Chem., Int. Ed*. **2012**, *51*, 5252–5255.

(44) Dalrymple, S. A.; Shimizu, G. K. H. Crystal Engineering of A Permanently Porous Network Sustained Exclusively by Charge-Assisted Hydrogen Bonds. *J. Am. Chem. Soc*. **2007**, *129*, 12114–12116.

(45) Jacobs, T.; Smith, V. J.; Thomas, L. H.; Barbour, L. J. Carbon Dioxide Entrapment in An Organic Molecular Host. *Chem. Commun*. **2014**, *50*, 85–87.

(46) Yang, W.; Greenaway, A.; Lin, X.; Matsuda, R.; Blake, A. J.; Wilson, C.; Lewis, W.; Hubberstey, P.; Kitagawa, S.; Champness, N. R.; Schröder, M. Exceptional Thermal Stability in A Supramolecular Organic Framework: Porosity and Gas Storage. *J. Am. Chem. Soc*. **2010**, *132*, 14457–14469.

(47) Bezzu, C. G.; Helliwell, M.; Warren, J. E.; Allan, D. R.; McKeown, N. B. Heme-Like Coordination Chemistry within Nanoporous Molecular Crystal. *Science* **2010**, *327*, 1627–1630.

(48) Lü, J.; Perez-Krap, C.; Suyetin, M.; Alsmail, N. H.; Yan, Y.; Yang, S.; Lewis, W.; Bichoutskaia, E.; Tang, C. C.; Blake, A. J.; Cao, R.; Schröder, M. A Robust Binary Supramolecular Organic Framework (SOF) with High $CO_2$ Adsorption and Selectivity. *J. Am. Chem. Soc*. **2014**, *136*, 12828−12831.

(49) Yang, W.; Li, B.; Wang, H.; Alduhaish, O.; Alfooty, K.; Zayed, M. A.; Li, P.; Arman, H. D.; Chen, B. A Microporous Porphyrin-Based Hydrogen-Bonded Organic Framework for Gas Separation. *Cryst. Growth Des*. **2015**, *15*, 2000−2004.

(50) Wang, H.; Li, B.; Wu, H.; Hu, T.-L.; Yao, Z.; Zhou, W.; Xiang, S.; Chen, B. A Flexible Microporous Hydrogen-Bonded Organic Framework for Gas Sorption and Separation. *J. Am. Chem. Soc*. **2015**, *137*, 9963−9970.

(51) Zhou, D.-D.; Xu, Y.-T.; Lin, R.-B.; Mo, Z.-W.; Zhang, W.-X.; Zhang, J.-P. High-Symmetry Hydrogen-Bonded Organic Frameworks: Air Separation and Crystal-to-Crystal Structural Transformation. *Chem. Commun*. **2016**, *52*, 4991–4994.

(52) Li, P.; He, Y.; Guang, J.; Weng, L.; Zhao, J. C.-G.; Xiang, S.; Chen, B. A Homochiral Microporous Hydrogen-Bonded Organic Framework for Highly Enantioselective Separation of Secondary Alcohols. *J. Am. Chem. Soc*. **2014**, *136*, 547−549.

(53) Song, Q.; Jiang, S.; Hasell, T.; Liu, M.; Sun, S.; Cheetham, A. K.; Sivaniah, E.; Cooper, A. I. Porous Organic Cage Thin Films and Molecular‐Sieving Membranes. *Adv. Mater*. **2016**, *28*, 2629–2637.

(54) Horiuchi, S.; Tokura, Y. Organic Ferroelectrics. *Nat. Mater*. **2008**, *7*, 357–366.

(55) Halik, M.; Klauk, H.; Zschieschang, U.; Schmid, G.; Dehm, C.; Schütz, M.; Maisch, S.; Effenberger, F.; Brunnbauer, M.; Stellacci, F. Low-Voltage Organic Transistors with An Amorphous Molecular Gate Dielectric. *Nature* **2004**, *431*, 963–966.

(56) Mutai, T.; Satou, H.; Araki, K. Reproducible On–Off Switching of Solid-State Luminescence by Controlling Molecular Packing Through Heat-Mode Interconversion. *Nat. Mater*. **2005**, *4*, 685–687.

(57) Mitschke, U.; Bäuerle, P. The Electroluminescence of Organic Materials. *J. Mater. Chem*. **2000**, *10*, 1471–1507.

(58) Tian, J.; Thallapally, P. K.; Dalgarno, S. J.; McGrail, P. B.; Atwood, J. L. Amorphous Molecular Organic solids for Gas adsorption. *Angew. Chem., Int. Ed*. **2009**, *48*, 5492–5495.

(59) Chiang, L.Y.; Wang, L.Y.; Swirczewski, J. W.; Soled, S.; Cameron, S. Efficient synthesis of Polyhydroxylated Fullerene Derivatives via Hydrolysis of Polycyclosulfated Precursors. *J. Org. Chem*. **1994**, *59*, 3960–3968.

(60) Kokubo, K.; Matsubayashi, K.; Tategaki, H.; Takada, H.; Oshima, T. Facile Synthesis of Highly Water-Soluble Fullerenes More Than Half-Covered by Hydroxyl Groups. *ACS Nano* **2008**, *2*, 327–333.

(61) Kokubo, K.; Shirakawa, S.; Kobayashi, N.; Aoshima, H.; Oshima, T. Facile and Scalable Synthesis of a Highly Hydroxylated Water-Soluble Fullerenol as A Single Nanoparticle. *Nano Res*. **2011**, *4*, 204–215.

(62) Takaya, Y.; Tachika, H.; Hayashi, T.; Kokubo, K.; Suzuki, K. Performance of Water-Soluble Fullerenol as Novel Functional Molecular Abrasive Grain for Polishing Nanosurfaces. *CIRP Ann.–Manuf. Techn.* **2009**, *58*, 495–498.

(63) Takaya, Y.; Kishida, H.; Hayashi, T.; Michihata, M.; Kokubo, K. Chemical Mechanical Polishing of Patterned Copper Wafer Surface Using Water-soluble Fullerenol Slurry. *CIRP Ann.–Manuf. Techn.* **2011**, *60*, 567–570.

(64) Usenko, Y.; Harper, S. L.; Tanguay, R. L. Fullerene $C_{60}$ Exposure Elicits an Oxidative Stress Response in Embryonic Zebrafish. *Toxicol. Appl. Pharmacol*. **2008**, *229*, 44–55.

(65) Cai, X.; Jia, H.; Liu, Z.; Hou, B.; Luo, C.; Feng, Z.; Li, W.; Liu, J. Polyhydroxylated Fullerene Derivative $C_{60}(OH)_{24}$ Prevents Mitochondrial Dysfunction and Oxidative Damage in An $MPP^+$ - Induced Cellular Model of Parkinson's Disease. *J. Neurosci. Res.* **2008**, *86*, 3622–3634.

(66) Inui, S.; Aoshima, H.; Ito, M.; Kokubo, K.; Itami, S. Inhibition of Sebum Production and Propionibacterium Acnes Lipase Activity by Fullerenol, A Novel Polyhydroxylated Fullerene: Potential as A Therapeutic Reagent for Acne. *J. Cosmet. Sci*. **2012**, *63*, 259–265.

(67) Saitoh, Y.; Mizuno, H.; Xiao, L.; Hyoudou, S.; Kokubo, K.; Miwa, N. Polyhydroxylated Fullerene $C_{60}(OH)_{44}$ suppresses Intracellular Lipid Accumulation Together With Repression of Intracellular Superoxide Anion Radicals and Subsequent PPARγ2 Expression During Spontaneous Differentiation of OP9 Preadipocytes Into Adipocytes. *Mol. Cell Biochem*. **2012**, *366*, 191–200.

(68) Aoshima, H.; Kokubo, K.; Shirakawa, S.; Ito, M.; Yamana, S.; Oshima, T. Antimicrobial Activity of Fullerenes and Their Hydroxylated Derivatives. *Biocontrol Sci*. **2009**, *14*, 69–72.

(69) Komatsu, K.; Murata, M.; Murata, Y. Encapsulation of Molecular Hydrogen in Fullerene $C_{60}$ by Organic Synthesis. *Science* **2005**, *307*, 238–240.

(70) Kurotobi, K.; Murata, Y. A Single Molecule of Water Encapsulated in Fullerene $C_{60}$. *Science* **2011**, *333*, 613–616.

(71) Futagoishi, T.; Murata, M.; Wakamiya, A.; Murata, Y. Trapping $N_2$ and $CO_2$ on The Sub-nano Scale in The Confined Internal Spaces of Open-Cage $C_{60}$ Derivatives: Isolation and Structural Characterization of the Host–Guest Complexes. *Angew. Chem., Int. Ed*. **2015**, *54*, 14791–14794.

(72) Kelty, S. P.; Chen, C.-C.; Lieber, C. M. Superconductivity at 30 K in Caesium-Doped $C_{60}$. *Nature* **1991**, *352*, 223–225.

(73) Ganin, A. Y.; Takabayashi, Y.; Khimyak, Y. Z.; Margadonna, S.; Tamai, A.; Rosseinsky, M. J.; Prassides, K. Bulk Superconductivity at 38 K in a Molecular System. *Nat. Mater*. **2008**, *7*, 367–71.

(74) Connolly, M. L. Computation of Molecular Volume. *J. Am. Chem. Soc*. **1985**, *107*, 1118-1124.

(75) Kao, K. C. *Dielectric Phenomena in Solids*; Elsevier: Amsterdam, 2004.

(76) You, Y. –M.; Liao, W. –Q.; Zhao, D.; Ye, H. –Y.; Zhang, Y.; Zhou, Q.; Niu, X.; Wang, J.; Li, P. –F.; Fu, D. –W.; Wang, Z.; Gao, S.; Yang, K.; Liu, J. –M.; Li, J.; Yan, Y.; Xiong, R. –G. An Organic-Inorganic Perovskite Ferroelectric with Large Piezoelectric Response. *Science*, **2017**, *357*, 306–309.

(77) Liao1, W. –Q.; Zhao, D.; Tang, Y. –Y.; Zhang, Y.; Li, P. –F.; Shi, P. –P.; Chen, X. –G.; You, Y. –M.; Xiong, R. –G. A Molecular Perovskite Solid Solution with Piezoelectricity Stronger Than Lead Zirconate Titanate. *Science* **2019**, *363*, 1206–1210.

(78) Huang, X.; Zhi, C.; Jiang, P.; Golberg, D.; Bando, Y. Tanaka, T. Temperature-Dependent Electrical Property Transition of Graphene Oxide Paper. *Nanotechnology*, **2012**, *23*, 455705−1−10.

(79) McDonald, T. M.; Lee, W. R.; Mason, J. A.; Wiers, B. M.; Hong, C. S.; Long, J. R. Capture of Carbon Dioxide From Air and Flue Gas in the Alkylamine-Appended Metal–Organic–Framework mmen-$Mg_2$(dobpdc). *J. Am. Chem. Soc*. **2012**, *134*, 7056−7065.

(80) Dunne, J. A.; Rao, M.; Sircar, S.; Gorte, R. J.; Myers, A. L. Calorimetric Heats of Adsorption and Adsorption Isotherms. 2. $O_2$, $N_2$, Ar, $CO_2$, $CH_4$, $C_2H_6$, and $SF_6$ on NaX, H-ZSM-5, and Na-ZSM-5 Zeolites. *Langmuir* **1996**, *12*, 5896−5904.

(81) Kauffman, K. L.; Culp, J. T.; Goodman, A.; Matranga. C. FT-IR Study of $CO_2$ Adsorption in a Dynamic Copper(II) Benzoate−Pyrazine Host with $CO_2$−$CO_2$ Interactions in the Adsorbed State. *J. Phys. Chem. C* **2011**, *115*, 1857−1866.

(82) Eguchi, R.; Uchida, S.; Mizuno, N. Computational Study of $CO_2$ Storage in Metal−Organic Frameworks. *J. Phys. Chem. C* **2012**, *116*, 16105−16110.

(83) Mihaylov, M.; Chakarova, K.; Andonova, S.; Drenchev, N.; Ivanova, E.; Sabetchadam, A.; Seoane, B.; Gascon, J.; Kapteijn, F.; Hadjiivanov, K. Adsorption Forms of $CO_2$ on MIL-53(Al) and $NH_2$-MIL-53(Al) as Revealed by FTIR Spectroscopy. *J. Phys. Chem. C* **2016**, *120*, 23584−23595.

(84) Garrone, E.; Bonelli, B.; Lamberti, C.; Civalleri, B.; Rocchia, M.; Roy, P.; Otero Areán, C. Carbon Dioxide ($C^{16}O_2$ and $C^{18}O_2$) Adsorption in Zeolite Y Materials: Effect of Cation, Adsorbed Water and Particle Size. *J. Chem. Phys*. **2002**, *117*, 10274−10282.

TOC Graphic